Tuning the Thermoelectric Performance of CaMnO$_3$-Based Ceramics by Controlled Exsolution and Microstructuring

Nikola Kanas,* Benjamin A. D. Williamson, Frank Steinbach, Richard Hinterding, Mari-Ann Einarsrud, Sverre M. Selbach, Armin Feldhoff, and Kjell Wiik

ACCESS | Metrics & More | Article Recommendations | Supporting Information

ABSTRACT: The thermoelectric properties of CaMnO$_{3-\delta}$/CaMn$_2$O$_4$ composites were tuned via microstructuring and compositional adjustment. Single-phase rock-salt-structured CaO−MnO materials with Ca:Mn ratios larger than unity were produced in reducing atmosphere and subsequently densified by spark plasma sintering in vacuum. Annealing in air at 1340 °C between 1 and 24 h activated redox-driven exsolution and resulted in a variation in microstructure and CaMnO$_{3-\delta}$ materials with 10 and 15 vol % CaMn$_2$O$_4$, respectively. The nature of the CaMnO$_{3-\delta}$/CaMn$_2$O$_4$ grain boundary was analyzed by transmission electron microscopy on short- and long-term annealed samples, and a sharp interface with no secondary phase formation was indicated in both cases. This was further complemented by density functional theory (DFT) calculations, which confirmed that the CaMnO$_{3-\delta}$ indeed is a line compound. DFT calculations predict segregation of oxygen vacancies from the bulk of CaMnO$_{3-\delta}$ to the interface between CaMnO$_{3-\delta}$ and CaMn$_2$O$_4$, resulting in an enhanced electronic conductivity of the CaMnO$_{3-\delta}$ phase. Samples with 15 vol % CaMn$_2$O$_4$ annealed for 24 h reached the highest electrical conductivity of 73 S·cm^{-1} at 900 °C. The lowest thermal conductivity was obtained for composites with 10 vol % CaMn$_2$O$_4$ annealed for 8 h, reaching 0.56 W·m^{-1}K^{-1} at 700 °C. However, the highest thermoelectric figure-of-merit, zT, was obtained for samples with 15 vol % CaMn$_2$O$_4$ reaching 0.11 at temperatures between 800 and 900 °C, due to the enhanced power factor above 700 °C. This work represents an approach to boost the thermoelectric performance of CaMnO$_{3-\delta}$ based composites.
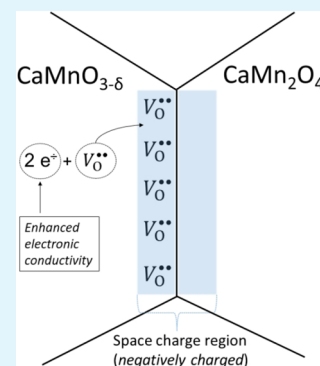
KEYWORDS: *oxide thermoelectrics, composite CaMnO$_{3-\delta}$, heterostructuring, electrical conductivity, thermal conductivity*

1. INTRODUCTION

Thermoelectric generators (TEGs) enable conversion of heat directly into electrical energy, representing a promising technology, which could contribute to the reduction in greenhouse gas emissions by increased efficiency of high-temperature processes, as well as to open ample opportunities in wireless sensor technologies.[1] TEGs combine materials with n- and p-type electronic conductivity and the efficiency is described by their figure-of-merit given in eq 1,

$$zT = \frac{S^2 \sigma T}{\kappa} \qquad (1)$$

where S is the Seebeck coefficient, κ is the thermal conductivity and σ the electrical conductivity.[2] According to eq 1, a high efficiency is favored by a high electronic conductivity and a large Seebeck coefficient combined with a low thermal conductivity, at elevated temperature. A simultaneous increase in both S and σ is challenging since an enhancement in σ usually is accompanied by a reduction in S.[3,4]

The most efficient approach to reduce the thermal conductivity is based on hierarchical phonon scattering, covering a wide range of wavelengths, which includes electron−phonon interaction, lattice distortion, introduction

of rattling fillers or point defects, precipitates, dislocations and increased concentration of grain boundaries.[5]

For high-temperature applications in ambient atmosphere the state-of-the-art metal-based thermoelectric devices are ruled out due to oxidation and melting and, due to their stability at elevated temperatures, oxides become a favorable choice. Oxides with p-type electronic conductivity combined with good thermoelectric properties are established,[4,6,7] while oxides with n-type electrical conductivity exhibit significantly lower thermoelectric performance. Among the promising oxide materials with n-type conductivity is CaMnO$_{3-\delta}$.[8] At oxidizing conditions, CaMnO$_{3-\delta}$ is a line compound and secondary phases such as Ruddlesden−Popper and spinel phases will form at nonunity molar ratios between Ca and Mn.[9] At reducing conditions solid solubility exists in the entire CaO−MnO composition range. This facilitates controlled synthesis of composite materials by presynthesizing single-phase
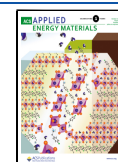
Table 1. Cation Ratios, Phase Composition, Annealing Time, and Nomenclature for Materials Investigated in This Study[a]

initial ratio n_{Ca}:n_{Mn}	rock-salt materials	nominal composition		annealing time (h) at 1340 °C in synthetic air	nomenclature
		vol % $CaMnO_{3-\delta}$	vol % $CaMn_2O_4$		
0.45:0.55	$Ca_{0.45}Mn_{0.55}O$	90	10	1	CMO10%1h
				4	CMO10%4h
				8	CMO10%8h
0.425:0.575	$Ca_{0.425}Mn_{0.575}O$	85	15	1	CMO15%1h
				4	CMO15%4h
				8	CMO15%8h
				24	CMO15%24h

[a]All samples obtained bulk densities between 96% and 98%. The theoretical densities of 4.58 and 4.59 g·cm^{-3} for CMO10% and CMO15% series, respectively, were calculated by the law of mixtures using the data for $CaMn_2O_4$ and $CaMnO_{3-\delta}$ from refs 23 and 24.

materials with various Ca:Mn ratios at reducing conditions followed by controlled exsolution of a secondary phase by further annealing at oxidizing conditions.[10] The formation of perovskite $CaMnO_3$ by thermally induced phase transformation from initial rock-salt structured CaMnO has also recently been reported in thin films by Ekström et al.[11,12] The stable structure of $CaMnO_{3-\delta}$ at ambient conditions is orthorhombic changing to tetragonal at 896 °C and cubic above 913 °C.[13] The phase transition between tetragonal and cubic is associated with enhancement in the electronic conductivity. In addition, tensile strain in $CaMnO_{3-\delta}$ heterostructures significantly favor the formation of oxygen vacancies.[14] Pronounced Jahn−Teller distortion at low and medium temperatures is characteristic for pure $CaMnO_{3-\delta}$, due to Jahn−Teller active high-spin d^4 Mn^{3+} ions charge compensating oxygen vacancies.

The zT values reported for pristine $CaMnO_{3-\delta}$ are typically below 0.10, such as 0.03[15] and 0.04[16] at 600 °C and 0.06[17] and 0.08[10] at 800 °C, whereas 0.12 at 800 °C has been reported[18] but not confirmed in other investigations. A giant power factor was reported for a $CaMnO_{3-\delta}$ sample fabricated by the laser floating-zone technique, reaching 0.39 mW·K^{-2}·m^{-1} at 800 °C.[19]

Recently, we reported a significant enhancement in electronic conductivity for a composite obtained by exsolution of 10 vol % $CaMn_2O_4$ (spinel) phase in a $CaMnO_{3-\delta}$ matrix. Although the $CaMn_2O_4$ secondary phase has a larger band gap of 1.89 eV,[20] compared to $CaMnO_{3-\delta}$ (see section 3.3.1), the overall electrical conductivity was observed to increase with increasing vol % of $CaMn_2O_4$.[10] The corresponding zT reached above 0.08 at 800 °C.[10] However, the origin of the enhanced electrical conductivity at low and medium temperatures was not explained. It was hypothesized that enhanced mobility or accumulation of charge carriers at the $CaMnO_{3-\delta}$/$CaMn_2O_4$ interfaces was responsible for the increased conductivity.

From this perspective, a further study was motivated and the variation in thermoelectric properties of $CaMnO_{3-\delta}$/$CaMn_2O_4$ composites was investigated by increasing the concentration of grain boundaries by grain size reduction and increasing the vol % of $CaMn_2O_4$ secondary phase from 10 to 15 vol %. The details of the interface between $CaMnO_{3-\delta}$ and $CaMn_2O_4$ were studied by transmission electron microscopy (TEM), and the variation in electrical properties was investigated by density functional theory (DFT) calculations.

The donor-substituted $CaMnO_3$ is usually demonstrating better thermoelectric performance than pristine $CaMnO_3$;[21,22] however, the main objective of the present study was to investigate the effect of heterointerfaces and microstructure on the thermoelectric properties in the pure Ca−Mn−O system.

To the best of our knowledge, no similar detailed study on tuning the thermoelectric performance of $CaMnO_{3-\delta}$/$CaMn_2O_4$ composites has been reported.

2. MATERIALS AND METHODS

2.1. Materials Synthesis. Synthesis of materials was based on an improved procedure published by Singh et al.[10] $CaCO_3$ (99.9%, Sigma-Aldrich) and MnO_2 (99.9%, Sigma-Aldrich) were mixed according to the following cation ratios n_{Ca}:n_{Mn} = 0.45:0.55 and n_{Ca}:n_{Mn} = 0.425:0.575, for simplicity denoted as $Ca_{0.45}Mn_{0.55}O$ and $Ca_{0.425}Mn_{0.575}O$, corresponding to composites with 10 and 15 vol % $CaMn_2O_4$, respectively. Estimated uncertainty of ±5 mg is expected due to the analytical balance limitation. The mixtures were ball milled with yttria stabilized zirconia balls in isopropanol for 4 h, followed by drying in a rotavapor (Buchi R-300). The dried mixtures were gently uniaxially pressed into pellets and heat-treated at 1050 °C in reducing atmosphere (5% H_2 in Ar) for 6 h to form single-phase materials with rock-salt structures. The pellets were crushed in a mortar, sieved, and planetary-milled for 30 min at 300 rpm prior to spark plasma sintering (SPS) in vacuum. Optimization of the sintering temperature was evaluated in the temperature range 875−1250 °C (Figure S1), and the optimum conditions to obtain dense rock-salt stuctured MnO−CaO ceramics (>96% relative densities) were assessed at 1000 °C, 75 MPa for 1 min dwell time, with heating rate of about 220 °C/min followed by a spontaneous cooling (power off). The dense materials were heat treated in a tube furnace in reducing atmosphere (5% H_2 in Ar) up to 850 °C, followed by a change to pure N_2 atmosphere and further heating up to 1340 °C and an isothermal hold for 1 h in order to reach thermal equilibrium. Once thermal equilibrium was established, N_2 gas was switched to synthetic air at isothermal conditions (1340 °C), initiating the redox-activated exsolution by oxygen exposure for 1, 4, 8, and 24 h, respectively, and the materials are accordingly referred to as CMO10%1h, CMO10%4h, CMO10%8h, CMO15%1h, CMO15%4h, CMO15%8h, and CMO15%24h (Table 1). Heating and cooling rates of 200 and 80 °C/h were used, respectively. CMO15%24h was prepared for scanning electron microscopy (SEM), TEM, and electrical conductivity measurements only.

2.2. Characterization. Phase purity of $Ca_{0.45}Mn_{0.55}O$ and $Ca_{0.425}Mn_{0.575}O$ rock-salt powders, sintered materials, and the final composites were characterized by X-ray diffraction (Bruker D8 DaVinci). Using Cu Kα radiation, the diffraction patterns were recorded in the 2θ range 20−75° with a scanning rate of 1°/min. All samples were finely ground prior to XRD analysis.

Particle size and morphology of the synthesized powders, as well as the microstructures of the bulk materials, were determined by SEM (Hitachi S-3400N).

Prior to SEM analysis, the ceramic composites were fine-polished with diamond suspension to 4 μm roughness and the polished surfaces were thermally etched at 1200 °C for 30 min and subsequently carbon coated. The grain size was estimated by the
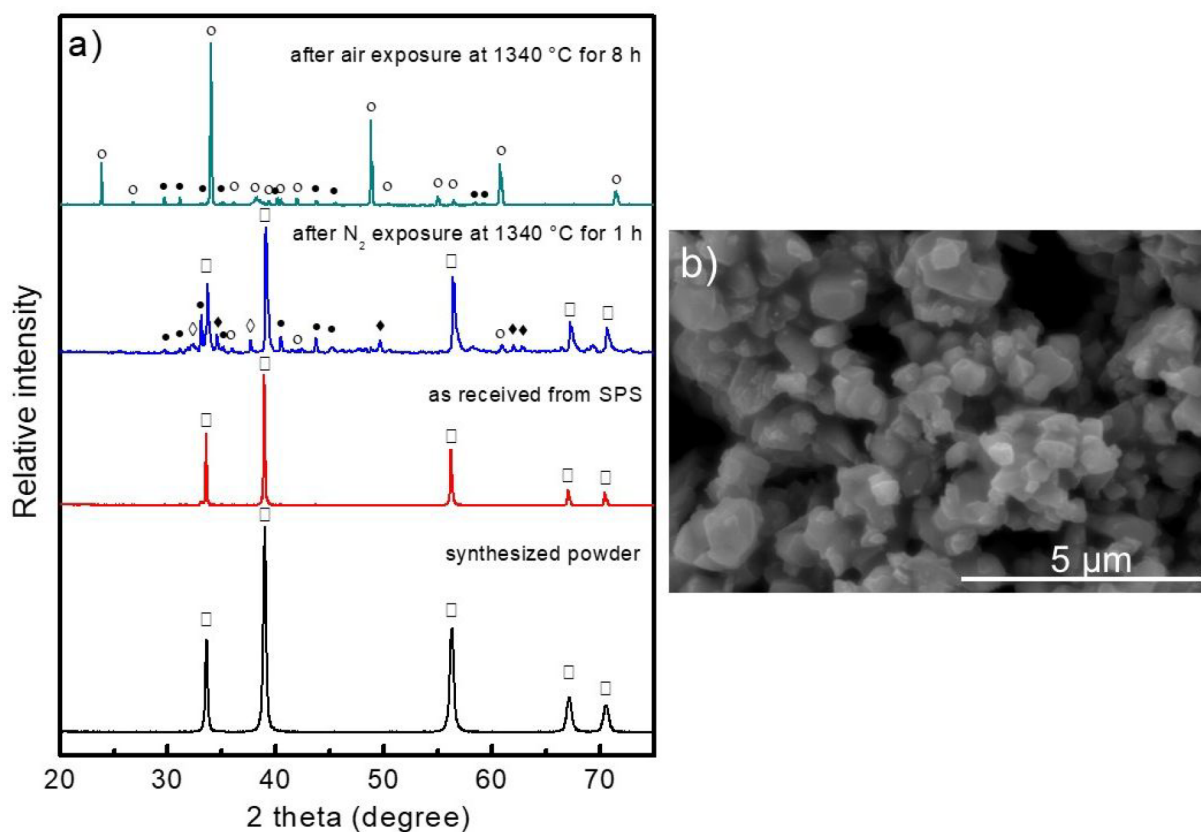
Figure 1. (a) X-ray diffraction patterns of synthesized rock-salt powder ($Ca_{0.45}Mn_{0.55}O$), ground rock-salt pellet as-received from SPS, ground SPS pellet annealed at 1340 °C for 1 h in N_2 and subsequently for 8 h in synthetic air: (□) rock salt (PDF 04-007-8378); (◇) Ruddlesden−Popper (PDF 00-018-0298); (○) perovskite (PDF 04-0148192); (●) spinel (PDF 04-015-3975). (b) SEM micrograph of rock-salt powder synthesized by the solid state method after planetary milling.

linear intercept method on about 9 grains, while the densities of the bulk samples were determined by the Archimedes method using isopropanol.

CMO10%1h and CMO15%24h were prepared for field-emission scanning electron microscopy (FE-SEM). The samples were polished on polymer-embedded diamond lapping films (DLF) followed by vibratory polisher (BuehlerVibroMet2) using 50 nm Al_2O_3 aqueous polishing suspension. Prior to FE-SEM analysis, the specimens were coated with a carbon layer of approximately 5−10 nm in thickness using carbon thread evaporation (Leica EM SCD500 device). FE-SEM micrographs and elemental distributions were recorded using an instrument of the type JEOL JSM-7610FPlus in secondary electron (SE) and back scatter electron (BSE) contrast combined with energy dispersive X-ray spectroscopy (EDXS) of the type Bruker XFlash 6/60 twin spectrometer.

For field-emission transmission electron microscopy (FE-TEM) using a JEOL JEM-2100F-UHR instrument at 200 kV, the samples were flat-polished from both sides on diamond lapping films (Allied High Tech, Techprep/Multiprep) and 3 kV argon-ion polished to electron transparency (Gatan, model 691 PIPS, precision ion polishing system). The FE-TEM was equipped with an energy-dispersive X-ray spectrometer of the type Oxford Instruments INCA 200 TEM and a Gatan imaging filter GIF 2001 for electron energy-loss spectroscopy (EELS) with emphasize on the energy-loss near-edge structure (ELNES). For scanning TEM (STEM), high-angular dark-field (HAADF) contrast was used.

All thermoelectric characterization was performed in synthetic air in the temperature range 300−900 °C with steps of 100 °C. Disk-shaped samples (∼12.5 mm diameter and ∼1.2 mm thickness) were prepared for thermal conductivity measurements (Netzsch, LFA 457 MicroFlash), while bar-shaped samples (∼15 mm × 3 mm × 4 mm) were prepared for simultaneous assessment of electrical conductivity (four-point method) and Seebeck coefficient in a Probostat (NorECs AS).

2.3. Computational Methods. DFT calculations were performed using the Vienna *ab initio* simulation package (VASP)[25−28] and PBEsol exchange−correlation functional.[29] The projector-augmented wave (PAW) method[30] was employed to describe the interactions between the core and the valence electrons. Self-interaction errors for Mn d-electrons were addressed by applying a Hubbard U of 3 eV,[29] following previous work on $CaMnO_{3-\delta}$.[32,33] Antiferromagnetic order on the Mn sublattices was imposed for both $CaMnO_{3-\delta}$ and $CaMn_2O_4$.[34−37]

Structural optimizations of bulk $CaMnO_{3-\delta}$ and $CaMn_2O_4$ were performed using plane-wave energy cut-offs of 500 eV and a Γ-centered *k*-point mesh of 4 × 4 × 3 and 4 × 3 × 1, respectively, allowing atomic positions and lattice vectors to relax until the forces on all the atoms were less than 0.01 eV Å^{-1}. Band alignment for $CaMnO_{3-\delta}$ and $CaMn_2O_4$ was performed by electronic relaxation of symmetric surface slabs terminated by (001) and (100) planes, respectively, with a bulk and vacuum width of 30 Å each. Hybrid functional (HSE06[38]) calculations were also performed to better understand the electronic structure and band alignment due to the typically improved electronic localization, particularly for O 2p states.[39−41] Surface slabs and analyses were performed using the open source Python3 package macrodensity,[42] while band structures and density of states (DOS) were plotted using sumo.[43]

3. RESULTS AND DISCUSSION

3.1. Phases, Microstructures, and Grain Boundaries.
Figure 1a shows X-ray diffraction patterns of synthesized $Ca_{0.45}Mn_{0.55}O$ powder, as-received from SPS, SPS sample
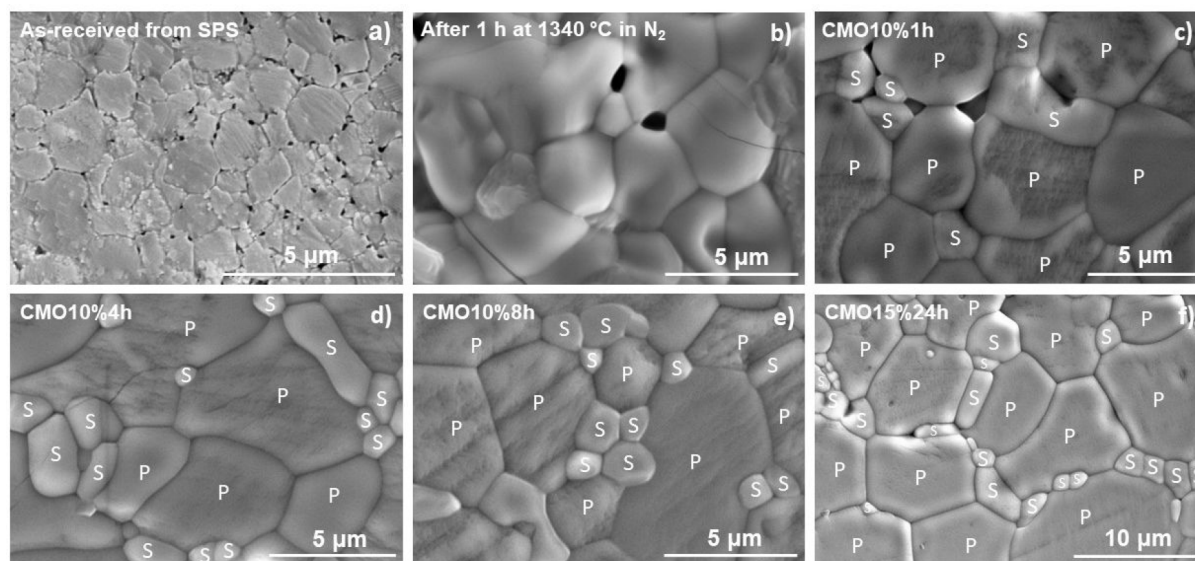
Figure 2. SEM micrographs (a) of rock-salt pellet as-received from SPS, (b) after 1 h annealing at 1340 °C in N_2, (c) after 1 h annealing in N_2 and 1 h in air at 1340 °C (CMO10%1h), (d) after 1 h annealing in N_2 and 4 h in air at 1340 °C (CMO10%4h), (e) after 1 h annealing in N_2 and 8 h in air at 1340 °C (CMO10%8h), and (f) after 1 h annealing in N_2 and 24 h in air at 1340 °C (CMO15%24h). Grains marked with "P" and "S" indicate perovskite and spinel phases, respectively.

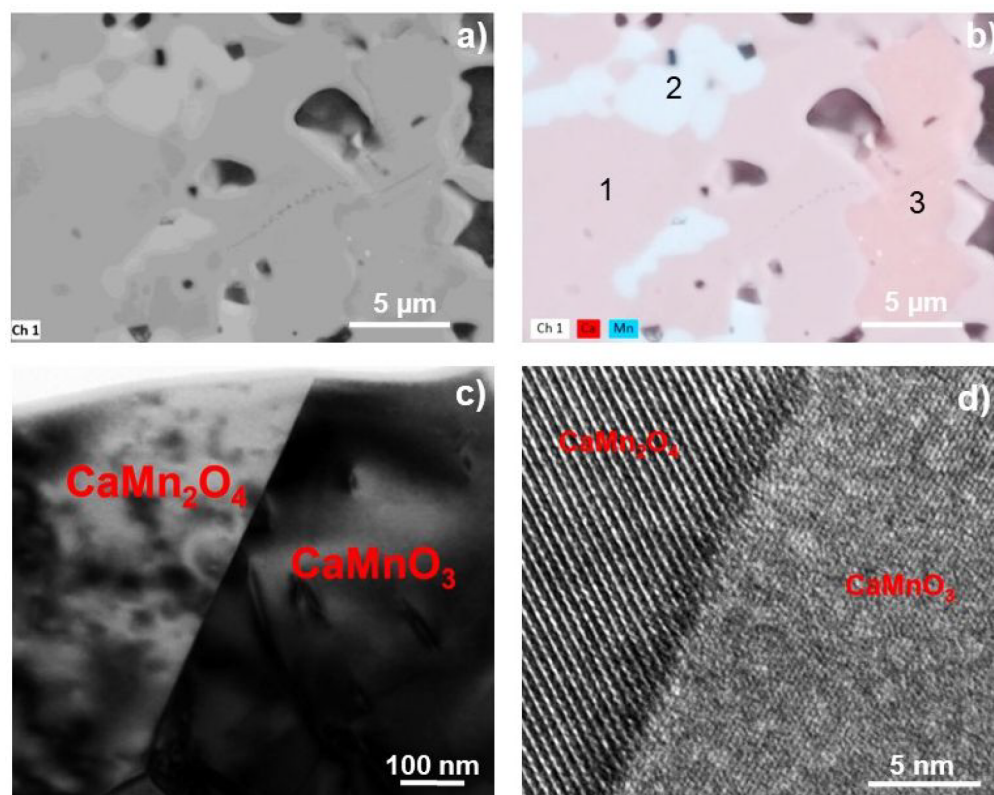**Figure 3.** Microstructural features of CMO10%1h. (a) SEM micrograph (back scatter) and (b) EDS mapping. Numbers 1, 2, and 3 indicate $CaMnO_{3-\delta}$, $CaMn_2O_4$, and $Ca_4Mn_3O_{10}$. (c) TEM-bright field image of a grain boundary region. (d) HRTEM of the interface between $CaMnO_{3-\delta}$ and $CaMn_2O_4$.

exposed to N_2 for 1 h at 1340 °C, and sample annealed in synthetic air at 1340 °C for 8 h (CMO10%8h), respectively.

The synthesized powder (in 5% H_2/Ar) and SPS pellet (in vacuum) shows the presence of phase pure $Ca_{0.45}Mn_{0.55}O$ rock-salt structure only, in accordance with the CaO−MnO phase diagram in reducing atmosphere.[9] However, the sample

exposed at 1340 °C for 1 h in N_2 also showed low-intensity diffraction lines of $CaMnO_{3-\delta}$ (perovskite), $CaMn_2O_4$ (spinel), and $Ca_4Mn_3O_{10}$ (Ruddlesden−Popper), due to a low partial pressure of oxygen in the N_2 atmosphere. Diffraction lines of $CaMnO_{3-\delta}$ and $CaMn_2O_4$ are present in the sample annealed for 8 h in synthetic air at 1340 °C
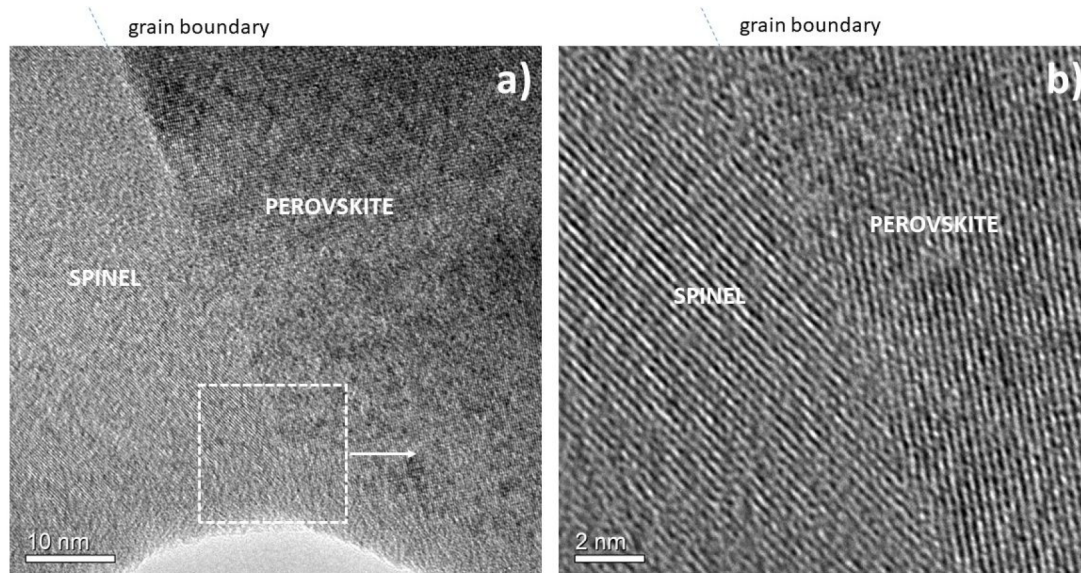
Figure 4. Grain boundary region between spinel $CaMn_2O_4$ and perovskite $CaMnO_{3-\delta}$ in CMO15%24h: (a) HRTEM micrograph and (b) magnified area of HRTEM micrograph. Dotted slash-line illustrates a direction of the interface between spinel $CaMn_2O_4$ and perovskite $CaMnO_{3-\delta}$.

showing that $Ca_4Mn_3O_{10}$ is transformed to perovskite and spinel on further annealing in oxidizing atmosphere. The SEM micrograph of the synthesized rock-salt powder in Figure 1b shows that submicrometer particles with a narrow particle size distribution was obtained by the solid-state synthesis. The same characteristic phase evolution and particle size were also observed (data not shown) for $Ca_{0.425}Mn_{0.575}O$ (15 vol % spinel).

The microstructure of the as-received pellet from SPS (Figure 2a) reveals a small and uniform grain size of about 0.9 μm; hence, only moderate grain growth is taking place during densification by SPS. Nanosized spherical pores are located at triple points and at grain boundaries.

The microstructure after 1 h at 1340 °C in N_2 (Figure 2b) is significantly different compared to the as-received sample from SPS. The grains are about 4 times larger, while the pores maintained their spherical shape, although somewhat expanded.

The microstructure of the sample CMO10%1h (Figure 2c) contains relatively uniform $CaMnO_{3-\delta}$ grains with an average size of about 4.5 μm, which indicates negligible grain growth after 1 h heat treatment in air at 1340 °C. Micrometer-sized grains of $CaMn_2O_4$ secondary phase form at triple points and at $CaMnO_{3-\delta}$ grain boundaries.

The microstructures of CMO10%4h (Figure 2d), CMO10%8h (Figure 2e), and CMO15%24h (Figure 2f) samples are similar except from the increasing grain size of the perovskite phase with increasing time, reaching approximately 5.8, 6.4, and 9.5 μm, respectively. The increase in grain growth with time is moderate and is anticipated to be hindered by the presence of the secondary spinel phase. More details of grain growth with time for the $CaMnO_{3-\delta}$ phase in CMO15% samples are presented later in the text.

CMO10%1h and CMO15%24h were subjected to a more detailed analysis by SEM-EDS analysis and further by STEM-HAADF, TEM-BF, SAED, TEM-bright field, and HRTEM.

Figure 3 shows microstructural features of CMO10%1h, whereas Figure 4 shows the characteristics of CMO15%24h sample. Figure 3a represents the SEM micrograph of the analyzed region where different areas (Figure 3b) marked with 1, 2, and 3 correspond to $CaMnO_{3-\delta}$, $CaMn_2O_4$, and $Ca_4Mn_3O_{10}$, in accordance with the XRD patterns in Figure 1a. $CaMnO_{3-\delta}$ and $CaMn_2O_4$ were the only phases observed in the CMO15%24h sample (Figure 4).

The grain boundaries formed between $CaMnO_{3-\delta}$ and $CaMn_2O_4$ in both CMO10%1h and CMO15%24h are sharp with no indication of a secondary phase (Figure 3c,d and Figure 4a,b). This supports the assumption that $CaMnO_{3-\delta}$ is a line compound with no solid solubility between $CaMnO_{3-\delta}$ and $CaMn_2O_4$.[9]

3.2. Thermoelectric Properties. *3.2.1. Electrical Conductivity.* The TE properties of investigated specimens were evaluated by characterizing σ, κ, and S. The electrical conductivity increases exponentially with temperature, as shown in Figure 5a,b, corresponding to a polaron hopping mechanism dominating at high temperatures. At temperatures below 600 °C the variation in σ between the samples is small, while a more pronounced variation is observed at higher temperatures, showing enhanced conductivity with increasing annealing time.

The highest electrical conductivity is observed for CMO15%24h reaching 73 S·cm^{-1} at 900 °C (Figure 5b), while the lowest is observed at 300 °C showing 3.5 S·cm^{-1} for CMO10%1h (Figure 5a). Figure 5c shows the isothermal electrical conductivities as a function of the $CaMnO_{3-\delta}$ grain size, while Figure 5d shows the variation in grain size for the $CaMnO_{3-\delta}$ phase as a function of annealing time at 1340 °C for the CMO15% samples. Energy difference across a curved grain boundary is determined as the dominating mechanism for $CaMnO_{3-\delta}$ grain growth (Figure S2). According to Figure 5c, the variation in isothermal electrical conductivity with grain size is small at temperatures below 700 °C whereas there is a pronounced enhancement at temperatures above 700 °C
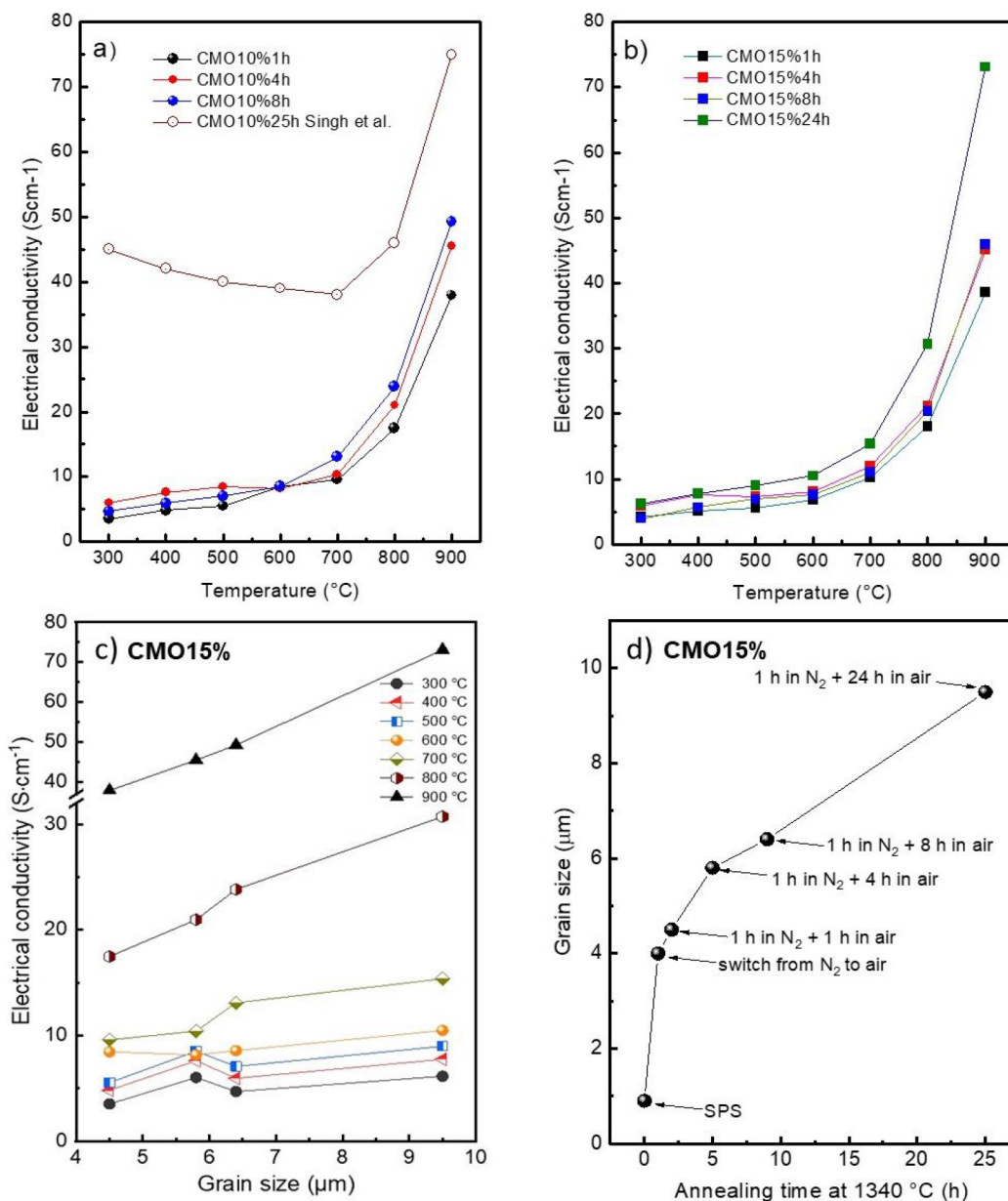
Figure 5. Electrical conductivity of (a) CMO10%1h, CMO10%4h, and CMO10%8h. Data from Singh et al., CMO10%25h,[10] are included for comparison. (b) CMO15%1h, CMO15%4h, CMO15%8h, and CMO15%24h as a function of temperature. (c) Isothermal electrical conductivity as a function of $CaMnO_{3-\delta}$ grain size in CMO15% samples. (d) Evolution of $CaMnO_{3-\delta}$ grain size in CMO15% samples as a function of annealing time at 1340 °C. At annealing time less than 1 h the reported grain size is for the $Ca_{0.425}Mn_{0.575}O$ rock-salt structure. Standard deviation of the conductivity measurements is below 3%.

where the electrical conductivity is dominated by polaron hopping. The density of grain boundaries will decrease with increasing grain size and, assuming that polaron hopping across grain boundaries is impeded, larger grains will enhance the electrical conductivity as given in Figure 5c.

Included in Figure 5a are also data reported by Singh et al.[10] for a $CaMnO_{3-\delta}$ composite with 10 vol % $CaMn_2O_4$ annealed in synthetic air for 25 h at 1350 °C (CMO10%25h), showing a significant enhancement in electrical conductivity at all temperatures below 900 °C compared to our CMO10% and CMO15% samples. This will be further commented in section 3.3.

3.2.2. Seebeck Coefficient and Power Factor. All the composites possess negative Seebeck coefficients over the whole temperature range, confirming that the major charge carriers are electrons; however, absolute values of the Seebeck coefficients are given in Figure 6a. For all the samples, the absolute value of the Seebeck coefficient increases with temperature up to about 500 °C followed by decreasing values at even higher temperatures. A maximum of 333 $\mu V \cdot K^{-1}$ at 500 °C, and a minimum of 60 $\mu V \cdot K^{-1}$ at 900 °C were reached for CMO10%8h and CMO10%4h, respectively. The reduction in Seebeck coefficient above 500 °C concides with the enhanced electrical conductivity given in Figure 5a,b and is explained by eq 2,[44]

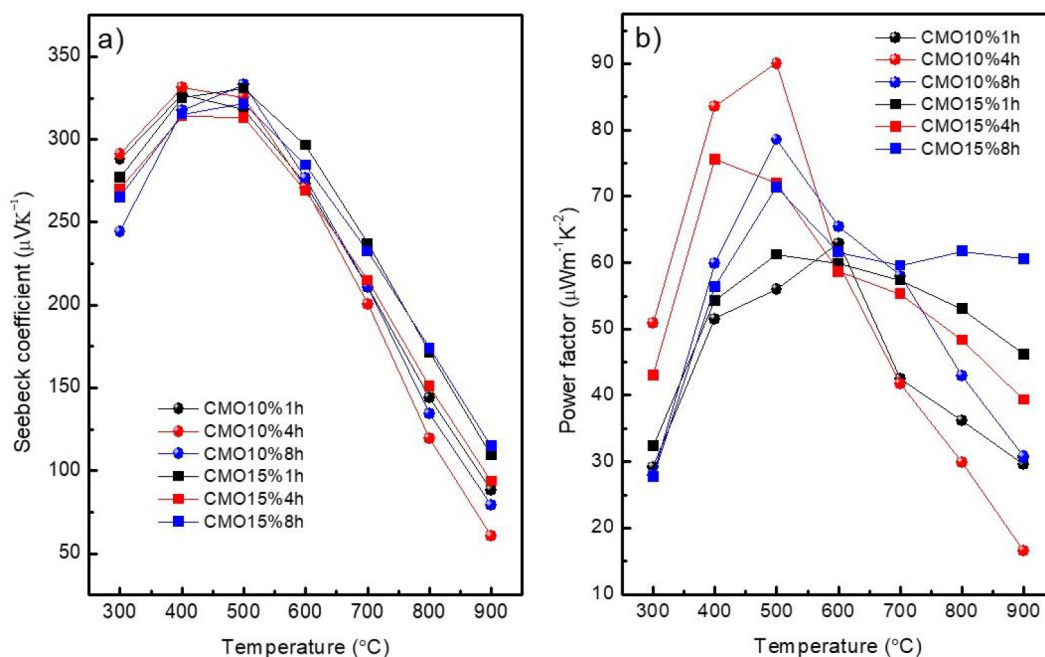$$S = \frac{8\pi^2 k_B^2}{3eh^2} m^* T \left(\frac{\pi}{3n} \right)^{2/3}$$

(2)

Figure 6. (a) Absolute values of Seebeck coefficients and (b) power factor of CaMnO$_3$-based composites as a function of temperature. Standard deviation of the Seebeck coefficient measurements is below 5%.

where k_B is the Boltzmann constant, e is the elementary charge, h is the Planck's constant, m^* is the effective mass of charge carrier, T is the absolute temperature, and n is the concentration of charge carriers. Hence, the Seebeck coefficient, S, is inversely proportional to the carrier concentration, $n^{2/3}$, corresponding to a decreasing S with increasing electronic conductivity.

The temperature dependence of the power factor, $S^2 \cdot \sigma$, is given in Figure 6b. The power factor is governed by the Seebeck coefficient as it follows the general trend of the Seebeck coefficient (Figure 6a) with the exception of CMO15%8h which shows an almost temperature-independent power factor at high temperatures, reaching a value of about 60 μW·m^{-1}·K^{-2}.

3.2.3. Thermal Conductivity and Figure-of-Merit. All the samples demonstrate low thermal conductivities over the whole temperature range, and the lowest is observed for samples annealed for 8 h (CMO10%8h and CMO15%8h) showing 0.56 W·m^{-1}·K^{-1} at 700 °C. In general, the thermal conductivity for any polycrystalline sample will increase with grain size due to less grain boundary scattering; however, the thermal conductivities shown in Figure 7a,b decrease with annealing time (except from the anomalous behavior of the sample CMO10%4h at low temperatures). This may be explained by the increasing volume fraction of spinel phase formed with increasing annealing time, corresponding to an enhanced density of CaMnO$_{3-\delta}$/CaMn$_2$O$_4$ interfaces which will effectively suppress the thermal conductivity by phonon scattering despite the increase in grain size. This emphasizes the importance of microstructure and distribution of the secondary phase in the composites with respect to controlling the thermal conductivity. The general trend of decreasing thermal conductivity with increasing temperature is expected due to the phonon mean free path being inversely proportional to the absolute temperature.[5]

The observed increase in thermal conductivity at temperatures above 700 °C can be explained by the electronic contribution. The thermal conductivity, κ_{tot}, is the algebraic sum of contribution from electrons, κ_{el}, and phonons (lattice vibrations), κ_p. κ_{el} can be calculated according to eq 3,

$$\kappa_{el} = \sigma \cdot T \cdot L \tag{3}$$

where σ is the total electrical conductivity (S·cm^{-1}), T the absolute temperature (K), and L is the Lorenz number (W·Ω·K^{-2})[45−47] which can be calculated by eq 4,

$$L = 1.5 + \exp(-|S|/116) \tag{4}$$

where S is the Seebeck coefficient.[48]

Figure 7c shows the thermal conductivities of CMO15%8h as a function of isothermal electrical conductivities. The decreasing thermal conductivity between 300 and 600 °C corresponds to the reduction in phonon mean free path with increasing temperature, and the electronic contribution, κ_{el}, calculated from eqs 3 and 4 is small due to the low electronic conductivity (inserted table in Figure 7c).

However, at temperatures above 700 °C the electronic contribution becomes significant and increases with temperature corresponding to 0.017 W·m^{-1}·K^{-1} (700 °C), 0.037 W·m^{-1}·K^{-1} (800 °C), and 0.104 W·m^{-1}·K^{-1} (900 °C). At 900 °C κ_{el} makes up approximately 15% of κ_{tot}.

Standard deviations for the Seebeck coefficient and electrical and thermal conductivity are approximately 5, 3, and 7%, respectively. The largest deviation is attributed to thermal conductivity because LFA measures specific heat *in situ* using an internal standard and calculates the thermal conductivity based on sample density and variation in density measured by dilatometer.

Figure 7d gives an overview of zT as a function of temperature for the CaMnO$_3$-based composites. The variations in zT between the composites are significant and most of the materials reach a maximum in zT between 500 and 700 °C except the CMO15%8h which demonstrates a maximum of 0.11 between 800 and 900 °C. The relatively modest power factor observed for CMO15%8h (Figure 6b) was compensated
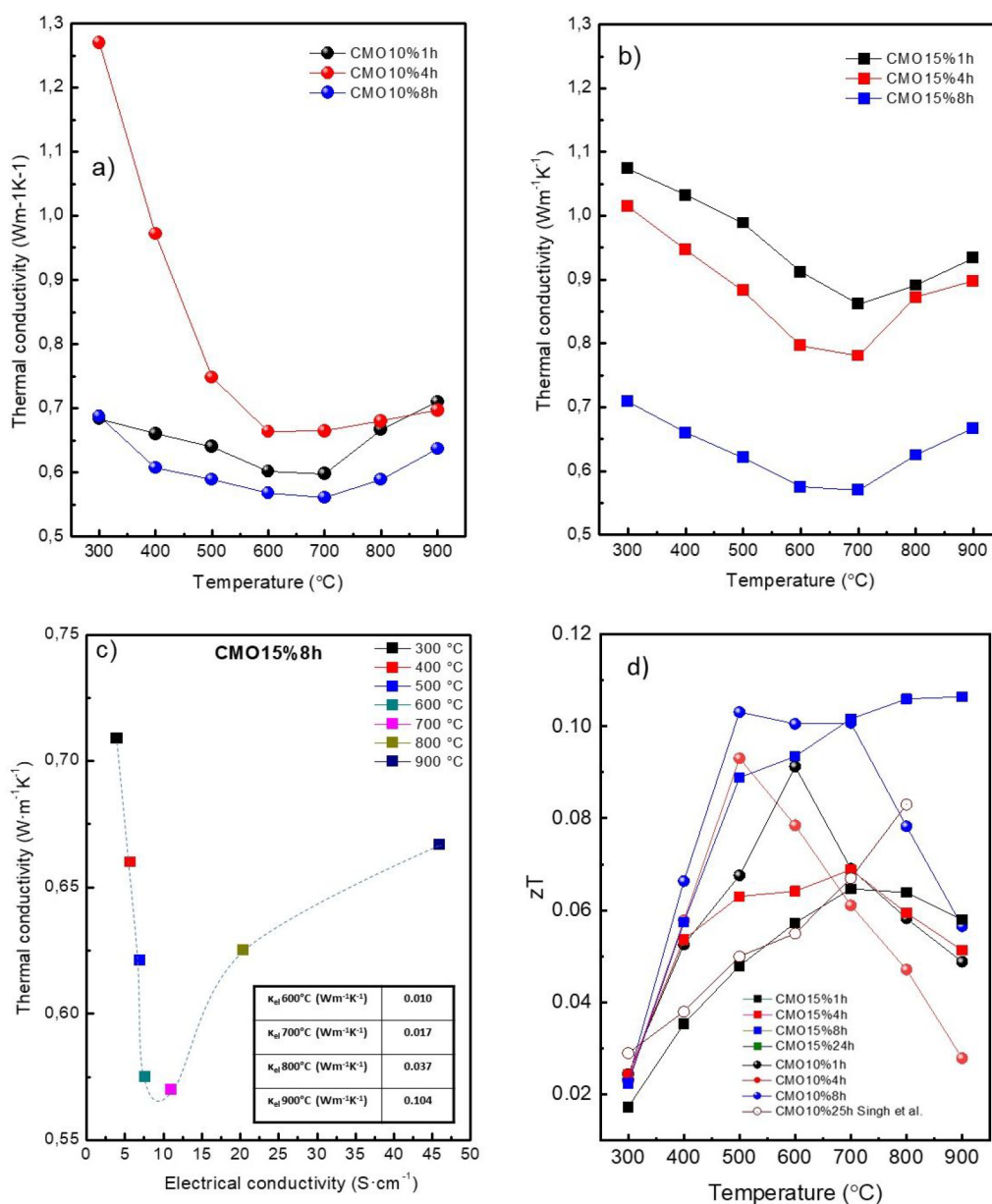
Figure 7. Thermal conductivity of (a) CMO10%1h, CMO10%4h, and CMO10%8h and (b) CMO15%1h, CMO15%4h, CMO15%8h as a function of temperature. (c) Thermal conductivity of CMO15%8h as a function of its isothermal electrical conductivities. An inserted table shows the contribution of the electronic part to thermal conductivity at 600, 700, 800, and 900 °C. (d) zT of the CaMnO$_3$-based composites as a function of temperature. Standard deviation of the thermal conductivity measurements is below 7%. The data from Singh et al.[10] are included for comparison.

by a significantly reduced thermal conductivity (Figure 7b) and resulted in materials with the highest zT reported so far in the literature for undoped CaMnO$_{3-\delta}$.

3.3. DFT Calculations. *3.3.1. Electronic Structure and Band Alignment.* We now turn to electronic structure calculations for CaMnO$_{3-\delta}$ and CaMn$_2$O$_4$ to investigate the intrinsic bulk charge transport properties of these phases. Electronic band structures and densities of states (DOS) for CaMnO$_{3-\delta}$ and CaMn$_2$O$_4$ are shown in Figure 8. A full comparison between HSE06 and PBEsol+U band structures is given in Figure S3, with band gaps and electron effective masses for CaMnO$_{3-\delta}$ and CaMn$_2$O$_4$ summarized in Tables S1 and S2, respectively. The calculated structural properties of both CaMnO$_{3-\delta}$ and CaMn$_2$O$_4$ are discussed in detail in the Supporting Information (Tables S3 and S4, respectively) and

both the PBEsol+U and the HSE06 functionals reproduce the experimental structural properties to within 1%.[26,27]

PBEsol+U gives indirect band gaps of 1.26 and 1.89 eV for CaMnO$_{3-\delta}$ and CaMn$_2$O$_4$, respectively (Figure 8a and Figure 8b), in agreement with experiments[28,29] and previous DFT studies.[30,31] In CaMnO$_{3-\delta}$ the valence band maximum (VBM) between X-Γ (Γ in HSE06) consists of both O 2p and Mn 3d states resulting in flat bands with highly localized holes, typical of mid-row transition metal oxides.[20,35] The conduction band minimum (CBM) at Γ consists mainly of Mn 3d states with a minor O 2p contribution.

The electron effective masses (Table S1) from Γ-Z, Γ-X, and Γ-Y are 1.42 m$_e$ (1.10 m$_e$), 0.48 m$_e$ (0.39 m$_e$), and 0.42 m$_e$ (0.35 m$_e$), respectively (HSE06 values are given in parentheses), implying polaronic conduction (type III: $m^* >$ 0.25 eV).[36]
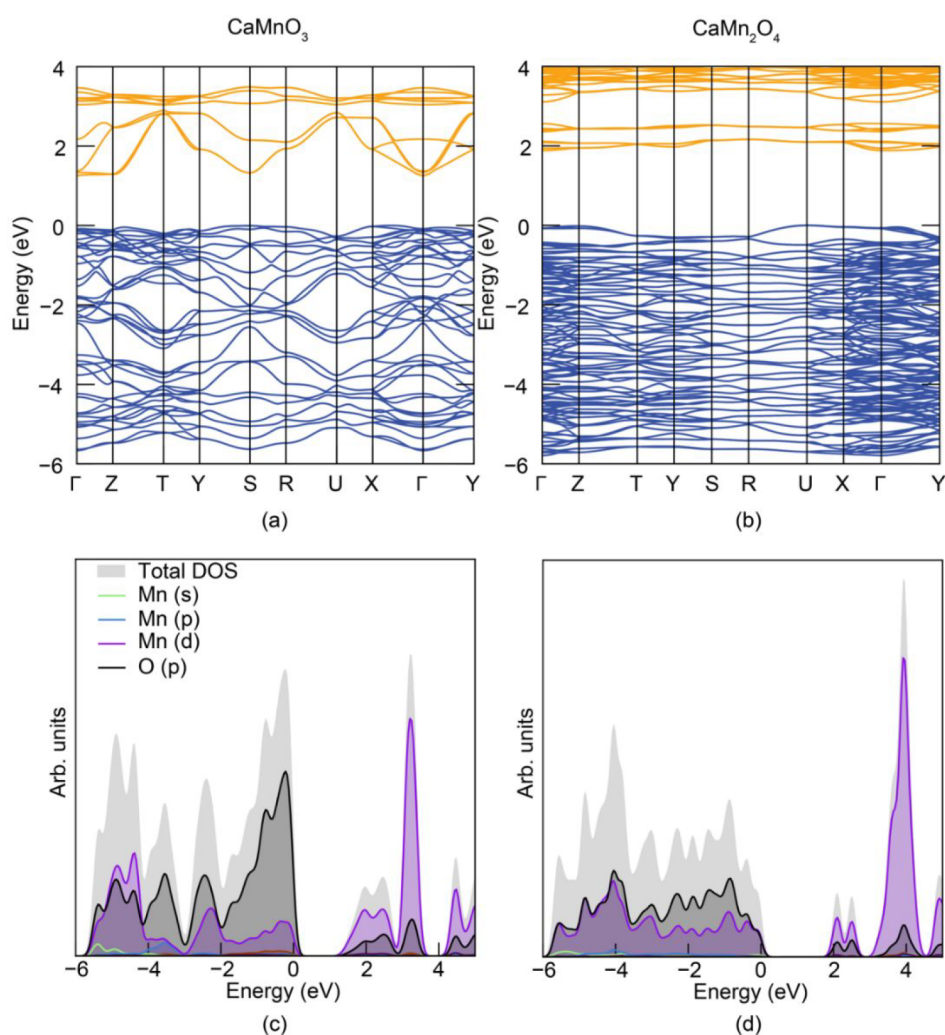
Figure 8. Calculated electronic band structures of (a) $CaMnO_{3-\delta}$ and (b) $CaMn_2O_4$ with blue valence bands and orange conduction bands. Corresponding densities of states (DOS) for (c) $CaMnO_{3-\delta}$ and (d) $CaMn_2O_4$. These calculations were done with the PBEsol functional. For clarity, only the spin-up component is shown as the spin-down component is symmetrical in these antiferromagnetic materials.

However, the more complex and distorted marokite structure of $CaMn_2O_4$ results in even less dispersed bands and more localized electrons with larger effective masses (4.38 m_e), $1.28m_e$ ($1.08\ m_e$), and $20.75\ m_e$ ($15.17\ m_e$) for the Γ-Z, Γ-X, and Γ-Y directions (HSE06 values) are given in parentheses. Hence, the calculated band gaps and effective electron masses show that $CaMnO_{3-\delta}$ is expected to be more conducting than $CaMn_2O_4$. The DOS for $CaMn_2O_4$ in Figure 8d shows the same O 2p and Mn 3d states at the VBM (U) for $CaMnO_{3-\delta}$ in Figure 8c, while Mn states dominate the CBM (Γ).

3.3.2. Trapped Oxygen Vacancies and Enhanced n-Type Conductivity. Bulk electronic band alignment for $CaMnO_{3-\delta}$ and $CaMn_2O_4$ is the basis for explaining the experimental electrical conductivity values. Band alignments for the (001) $CaMnO_{3-\delta}$ surface and the $CaMn_2O_4$ (100) surfaces as calculated with PBEsol+U are shown in Figure 9. HSE06 and PBEsol+U band alignment are compared in Figure S4.

The alignment of the VBM and CBM of the two materials across an interface allows the relative defect and electronic energetics of each material to be approximated. This concept has been successfully applied to understanding the electron–hole separation lifetimes in rutile and anatase TiO_2.[48] In
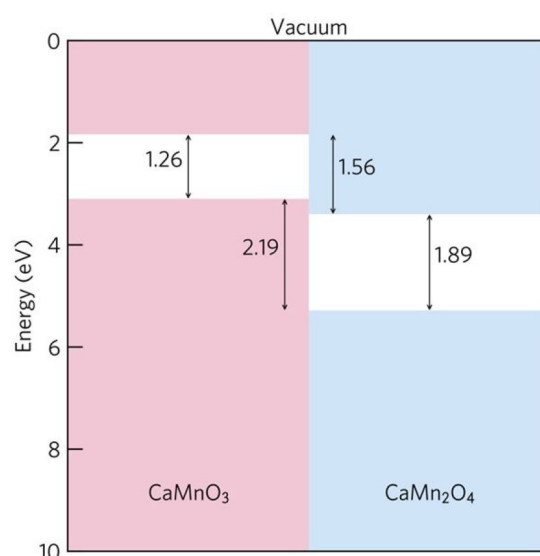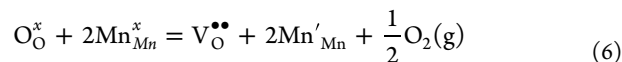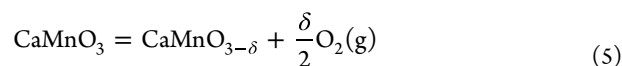

Figure 9. Bulk electronic band alignment of $CaMnO_{3-\delta}$ and $CaMn_2O_4$ using the 001 and 100 surface cuts, respectively, and the PBEsol+U functional.

general, n-type defects show preferential formation in materials with a higher electron affinity (low-lying CBM) and defects within a low ionization potential (high VBM);[48] thus the relative formation enthalpy of the oxygen vacancies, $V_O^{\bullet\bullet}$, between $CaMnO_{3-\delta}$ and $CaMn_2O_4$ can be predicted, e.g, following Yang et al.[48] Across an electronic band discontinuity there will be a large electrostatic gradient which favors segregation of specific types of defects at the interface.

The calculations show that the CBM is higher in energy for $CaMnO_{3-\delta}$ than for $CaMn_2O_4$ (1.09 and 1.56 eV, respectively) resulting in a significant electrostatic gradient. Following Yang et al.,[48] we predict segregation of $V_O^{\bullet\bullet}$ from the bulk of $CaMnO_{3-\delta}$ to the interface toward $CaMn_2O_4$ where the electrostatic gradient also helps trap oxygen vacancies at the interface. This segregation of $V_O^{\bullet\bullet}$ leaves uncompensated reduced Mn^{3+} in the bulk of $CaMnO_{3-\delta}$, predicted to result in an enhanced n-type conductivity upon prolonged annealing in air. This prediction is supported by the CMO10% series (Figure 5a) and the CMO15% series (Figure 5b). With increasing annealing time, the amount of exsoluted $CaMn_2O_4$ will increase (Figure 2c−f) and the electronic conductivity given in Figure 5a,b increases with annealing time. Hence, it is proposed that enhanced conductivity with annealing time is due to a combination of grain growth and trapping of oxygen vacancies at the perovskite/spinel interface. Of particular interest is the difference in electronic conductivity between CMO10%25h reported by Singh et al.[10] (Figure 5a) and CMO15%24h (Figure 5b). Both samples were annealed for a long time, and both reached an average grain of size of the $CaMnO_{3-\delta}$ phase of approximately 10 μm. However, the electronic conductivity reported for CMO10%25h is significantly higher than observed for CMO15%24h below 900 °C. Whereas the $CaMn_2O_4$ phase is exsoluted at triple points and some grain boundaries (Figure 2f), the resulting microstructure in the CMO10%25h is different showing that each $CaMnO_{3-\delta}$ grain is embedded in the exsoluted $CaMn_2O_4$ phase. It is anticipated that the oxygen vacancies are more effectively trapped at the interface when the spinel phase is evenly distributed around each perovskite grain resulting in a significant increase in the electronic conductivity, as opposed to the more random distribution observed in the CMO15%24h sample. This emphasizes the importance of microstructuring and distribution of the secondary phase in the composites with respect to controlling both thermal and electrical conductivities in these types of materials. Hence, the seemingly counterintuitive increase in electrical conductivity by incorporating less conducting $CaMn_2O_4$ can be explained from this interface segregation mechanism, which leaves the interface less conducting and bulk $CaMnO_{3-\delta}$ more conducting. The samples were annealed at 1340 °C in synthetic air, and disregarding at first the formation of the spinel phase, we may assume that equilibrium with the partial pressure of oxygen (pO_2) in the atmosphere (0.2 atm) is established according to eq 5. That is, a certain concentration of oxygen vacancies $[V_O^{\bullet\bullet}]$ is established in the $CaMnO_3$ phase as described by eq 6. However, with increasing annealing time at 1340 °C the concentration of $CaMnO_3/CaMn_2O_4$ interfaces will increase due to the continuous exsolution of the spinel phase at high temperatures. Given that there is a driving force for migration of oxygen vacancies to the interface (electrostatic gradient) and that the interface traps the oxygen vacancies, the oxygen vacancy concentration $[V_O^{\bullet\bullet}]$ in the $CaMnO_3$ bulk phase will be diminished. Assuming eq 2 at equilibrium, a diminution in

$[V_O^{\bullet\bullet}]$ must be compensated by an increased concentration of Mn^{3+} on Mn-sites $[Mn'_{Mn}]$, when pO_2 in the ambient atmosphere remains the same.

$$CaMnO_3 = CaMnO_{3-\delta} + \frac{\delta}{2}O_2(g) \tag{5}$$

$$O_O^x + 2Mn_{Mn}^x = V_O^{\bullet\bullet} + 2Mn'_{Mn} + \frac{1}{2}O_2(g) \tag{6}$$

Our simple approach above also poses new challenges as the uncompensated formation of Mn'_{Mn} (Mn^{3+} on Mn-site, $Mn_{Mn}^x = Mn^{4+}$ on Mn-site) would negatively charge the $CaMnO_3$ grains while the grain boundaries become increasingly positive. How this will affect the electronic conductivity is not easily answered based on the present data.

The $CaMnO_3/CaMn_2O_4$ composites represent a promising high-temperature n-type oxide material for waste heat harvesting at elevated temperatures in applications related to finite heat sources,[4] and our investigation has shown that the thermoelectric properties may be enhanced by careful control of the microstructure. A natural extension of this work would be to add another parameter, such as an appropriate dopant, to enhance the thermoelectric performance even more.

4. CONCLUSIONS

$CaMnO_3$-based composites were successfully fabricated by solid state synthesis of rock-salt $Ca_{0.45}Mn_{0.55}O$ and $Ca_{0.425}Mn_{0.575}O$ powders in 5% H_2/Ar, followed by spark plasma sintering in vacuum and thermal annealing in synthetic air at 1340 °C between 1 and 24 h. This resulted in bulk ceramics with nominal compositions 10 and 15 vol % of $CaMn_2O_4$, bulk densities above 96%, and grain size between 5 and ∼10 μm, depending on the annealing time. The electrical conductivity of the ceramic composites increased with annealing time as a result of increased $CaMnO_{3-\delta}$ grain size combined with an oxygen vacancy trapping mechanism predicted by DFT calculations. The thermal conductivity decreased with increasing annealing time due to enhanced phonon scattering at the interface between $CaMn_2O_4$ and $CaMnO_{3-\delta}$. The highest zT was obtained for samples with 15 vol % $CaMn_2O_4$ (CMO15%8h) reaching 0.11 at temperatures between 800 and 900 °C. The obtained zT is the highest reported for undoped $CaMnO_{3-\delta}$. Enhanced electronic conductivity due to trapping of oxygen vacancies at the inteface between $CaMnO_{3-\delta}$ and $CaMn_2O_4$ represents a novel approach to boost the thermoelectric performance of $CaMnO_3$-based composites.

■ ASSOCIATED CONTENT

ⓈI Supporting Information

The Supporting Information is available free of charge at https://pubs.acs.org/doi/10.1021/acsaem.2c02012.

> Relative densities of spark plasma sintered rock-salt materials as a function of temperature, graphic of the grain growth mechanism dominated by the energy difference across a curved grain boundary, band structures of $CaMnO_3$ and $CaMn_2O_4$ using the DFT calculations, and information on band gaps and structure parameters (PDF)

■ AUTHOR INFORMATION

Corresponding Author

Nikola Kanas − *Department of Materials Science and Engineering, NTNU Norwegian University of Science and Technology, 7491 Trondheim, Norway; Institute BioSense, University of Novi Sad, 21000 Novi Sad, Serbia;* ● orcid.org/0000-0001-7906-7862; Email: nikola.kanas@biosense.rs

Authors

Benjamin A. D. Williamson − *Department of Materials Science and Engineering, NTNU Norwegian University of Science and Technology, 7491 Trondheim, Norway;* ● orcid.org/0000-0002-6242-1121

Frank Steinbach − *Institute of Physical Chemistry and Electrochemistry, Leibniz University Hannover, 30167 Hannover, Germany*

Richard Hinterding − *Institute of Physical Chemistry and Electrochemistry, Leibniz University Hannover, 30167 Hannover, Germany;* ● orcid.org/0000-0002-7604-4582

Mari-Ann Einarsrud − *Department of Materials Science and Engineering, NTNU Norwegian University of Science and Technology, 7491 Trondheim, Norway;* ● orcid.org/0000-0002-3017-1156

Sverre M. Selbach − *Department of Materials Science and Engineering, NTNU Norwegian University of Science and Technology, 7491 Trondheim, Norway;* ● orcid.org/0000-0001-5838-8632

Armin Feldhoff − *Institute of Physical Chemistry and Electrochemistry, Leibniz University Hannover, 30167 Hannover, Germany;* ● orcid.org/0000-0003-1599-432X

Kjell Wiik − *Department of Materials Science and Engineering, NTNU Norwegian University of Science and Technology, 7491 Trondheim, Norway*

Complete contact information is available at:
https://pubs.acs.org/10.1021/acsaem.2c02012

Notes

The authors declare no competing financial interest.

■ REFERENCES

(1) Verma, G.; Sharma, V. A novel thermoelectric energy harvester for wireless sensor network application. *IEEE Trans. Ind. Electon.* **2019**, *66*, 3530−3538.

(2) Ioffe, A. *Semiconductor Thermoelements and Thermoelectric Cooling*, 1st ed.; Infosearch Ltd.: London, 1957.

(3) Narducci, D. Do we really need high thermoelectric figure of merit? A critical appraisal to the power conversion efficiency of thermoelectric materials. *Appl. Phys. Lett.* **2011**, *99*, 102104.

(4) Bittner, M.; Kanas, N.; Hinterding, R.; Steinbach, F.; Räthel, J.; Schrade, M.; Wiik, K.; Einarsrud, M.-A.; Feldhoff, A. A comprehensive study on improved power materials for high-temperature thermoelectric generators. *J. Power Sources.* **2019**, *410*, 143−151.

(5) Fu, C.; Wu, H.; Liu, Y.; He, J.; Zhao, X.; Zhu, T. Enhancing the figure of merit of heavy-band thermoelectric materials through hierarchical phonon scattering. *Adv. Sci.* **2016**, *3*, 1600035.

(6) Shikano, M.; Funahashi, R. Electrical and thermal properties of single-crystalline $(Ca_2CoO_3)_{0.7}CoO_2$ with a $Ca_3Co_4O_9$ structure. *Appl. Phys. Lett.* **2003**, *82*, 1851−1853.

(7) Wu, N.; Holgate, T. C.; Nong, N. V.; Pryds, N.; Linderoth, S. High temperature thermoelectric properties of $Ca_3Co_4O_{9+\delta}$ by auto-combustion synthesis and spark plasma sintering. *J. Eur. Ceram. Soc.* **2014**, *34*, 925−931.

(8) Bocher, L.; Aguirre, M. H.; Logvinovich, D.; Shkabko, A.; Robert, R.; Trottmann, M.; Weidenkaff, A. $CaMn_{1-x}Nb_xO_3$ ($x \leq 0.08$) perovskite-type phases as promising new high-temperature n-type thermoelectric materials. *Inorg. Chem.* **2008**, *47*, 8077−8085.

(9) Horowitz, H. S.; Longo, J. M. Phase relations in the Ca-Mn-O system. *Mater. Res. Bull.* **1978**, *13*, 1359−1369.

(10) Singh, S. P.; Kanas, N.; Desissa, T. D.; Einarsrud, M.-A.; Norby, T.; Wiik, K. Thermoelectric properties of non-stoichiometric $CaMnO_{3-\delta}$ composites formed by redox-activated exsolution. *J. Eur. Ceram. Soc.* **2020**, *40*, 1344−1351.

(11) Ekström, E.; le Febvrier, A.; Fournier, D.; Lu, J.; Ene, V.-L.; Van Nong, N.; Eriksson, F.; Eklund, P.; Paul, B. Formation mechanism and thermoelectric properties of $CaMnO_3$ thin films synthesized by annealing of $Ca_{0.5}Mn_{0.5}O$ films. *J. Mater. Sci.* **2019**, *54*, 8482−8491.

(12) Ekström, E.; le Febvrier, A.; Bourgeois, F.; Lundqvist, B.; Palisaitis, J.; Persson, P. O. Å.; Caballero-Calero, O.; Martín-González, M. S.; Klarbring, J.; Simak, S. I.; Eriksson, F.; Paul, B.; Eklund, P. The effects of microstructure, Nb content and secondary Ruddlesden-Popper phase on thermoelectric properties in perovskite $CaMn_{1-x}Nb_xO_3$ (x = 0-0.10) thin films. *RSC Adv.* **2020**, *10*, 7918−7926.

(13) Taguchi, H.; Nagao, M.; Sato, T.; Shimada, M. High-temperature phase transition of $CaMnO_{3-\delta}$. *J. Solid State Chem.* **1989**, *78*, 312−315.

(14) Aschauer, U.; Pfenninger, R.; Selbach, S. M.; Grande, T.; Spaldin, N. A. Strain-controlled oxygen vacancy formation and ordering in $CaMnO_3$. *Phys. Rev. B* **2013**, *88*, 054111.

(15) Torres, S. O. A.; Thomazini, D.; Balthazar, G. P.; Gelfuso, M. V. Microstructural influence on thermoelectric properties of $CaMnO_3$ ceramics. *Mater. Res.* **2020**, *23*, 20200169.

(16) Flahaut, D.; Funahashi, R.; Lee, K.; Ohta, H.; Koumoto, K. Effect of the Yb substitutions on the thermoelectric properties of $CaMnO_3$. *25th International Conference on Thermoelectrics*; IEEE: Vienna, 2006; pp 103−106.

(17) Zhu, Y. H.; Su, W. B.; Liu, J.; Zhou, Y. C.; Li, J.; Zhang, X.; Du, Y.; Wang, C. L. Effect of Dy and Yb co-doping on the thermoelectric properties of $CaMnO_3$ ceramics. *Ceram. Int.* **2015**, *41*, 1535−1539.

(18) Thiel, P.; Eilertsen, J.; Populoh, S.; Saucke, G.; Döbeli, M.; Shkabko, A.; Sagarna, L.; Karvonen, L.; Weidenkaff, A. Influence of tungsten substitution and oxygen deficiency on the thermoelectric properties of $CaMnO_{3-\delta}$. *J. Appl. Phys.* **2013**, *114*, 243707.

(19) Ferreira, N. M.; Neves, N. R.; Ferro, M. C.; Torres, M. A.; Madre, M. A.; Costa, F. M.; Sotelo, A.; Kovalevsky, A. V. Growth rate effects on the thermoelectric performance of $CaMnO_3$-based ceramics. *J. Eur. Ceram. Soc.* **2019**, *39*, 4184−4188.

(20) Wu, X.-W.; Zhang, H.-X.; Liu, X.-J.; Zhang, X.-G. Optical properties and photocatalytic activity of marokite-type $CaMn_2O_4$. *Chin. Phys. Lett.* **2011**, *28*, 107101.

(21) Bocher, L.; Aguirre, M. H.; Logvinovich, D.; Shkabko, A.; Robert, R.; Trottmann, M.; Weidenkaff, A. $CaMn_{1-x}Nb_xO_3$ ($x \leq 0.08$) perovskite-type phases as promising new high-temperature n-type thermoelectric materials. *Inorg. Chem.* **2008**, *47*, 8077−8085.

(22) Zhu, Y.-H.; Su, W.-B.; Liu, J.; Zhou, Y.-C.; Li, J.; Zhang, X.; Du, Y.; Wang, C.-L. Effects of Dy and Yb co-doping on thermoelectric properties of $CaMnO_3$ ceramics. *Ceram. Int.* **2015**, *41*, 1535−1539.

(23) Zouari, S.; Ranno, L.; Cheikh-Rouhou, A.; Isnard, O.; Pernet, M.; Wolfers, P.; Strobel, P. New model for the magnetic structure of the marokite-type oxide $CaMn_2O_4$. *J. Alloys Compd.* **2003**, *353*, 5−11.

(24) Nakade, K.; Hirota, K.; Kato, M.; Taguchi, H. Effect of the Mn^{3+} ion on electrical and magnetic properties of orthorhombic perovskite-type $Ca(Mn_{1-x}Ti_x)O_{3-\delta}$. *Mater. Res. Bull.* **2007**, *42*, 1069−1076.

(25) Kresse, G.; Hafner, J. Ab-initio molecular dynamics for liquid metals. *Phys. Rev. B* **1993**, *47*, 558−561.

(26) Kresse, G.; Hafner, J. Ab-initio molecular-dynamics simulation of the liquid-metal amorphous-semiconductor transition in germanium. *Phys. Rev. B* **1994**, *49*, 14251−14269.

(27) Kresse, G.; Furthmuller, J. J. F. Efficient iterative schemes for ab-initio total-energy calculations using a plane-waveb basis set. *Phys. Rev. B: Condens. Matter Mater. Phys.* **1996**, *54*, 11169.

(28) Kresse, G.; Furthmüller, J. Efficiency of ab-initio total energy calculations for metals and semiconductors using a plane-wave basis set. *Comput. Mater. Sci.* **1996**, *6*, 15−50.

(29) Perdew, J. P.; Burke, K.; Ernzerhof, M. Generalized gradient approximation made simple. *Phys. Rev. Lett.* **1996**, *77*, 3865−3868.

(30) Blochl, P. E. Projector augmented-wave method. *Phys. Rev. B* **1994**, *50*, 17953−17979.

(31) Dudarev, S. L.; Botton, G. A.; Savrasov, S. Y.; Humphreys, C. J.; Sutton, A. P. Electron-energy-loss spectra and the structural stability of nickel oxide: An LSDA+U study. *Phys. Rev. B* **1998**, *57*, 1505−1509.

(32) Marthinsen, A.; Faber, C.; Aschauer, U.; Spaldin, N. A.; Selbach, S. M. Coupling and competition between ferroelectricity, magnetism, strain, and oxygen vacancies in $AMnO_3$ perovskites. *MRS Commun.* **2016**, *6*, 182−191.

(33) Marthinsen, A.; Grande, T.; Selbach, S. M. Microscopic link between electron localization and chemical expansion in $AMnO_3$ and $ATiO_3$ perovskites (A = Ca, Sr, Ba). *J. Phys. Chem. C* **2020**, *124*, 12922−12932.

(34) Hamdad, N.; Bouhafs, B. Theoretical analysis of the spin effect on the electronic and magnetic properties of the calcium manganese oxide $CaMnO_3$: GGA+U Calculation. *Physica B: Condensed Matter.* **2010**, *405*, 4595−4606.

(35) Poeppelmeier, K. R.; Leonowicz, M. E.; Scanlon, J. C.; Longo, J. M.; Yelon, W. B. Structure determination of $CaMnO_3$ and $CaMnO_{2.5}$ by X-Ray and neutron methods. *J. Solid State Chem.* **1982**, *45*, 71−79.

(36) Ling, C. D.; Neumeier, J. J.; Argyriou, D. N. Observation of antiferromagnetism in marokite $CaMn_2O_4$. *J. Solid State Chem.* **2001**, *160*, 167−173.

(37) Zouari, S.; Ranno, L.; Cheikh-Rouhou, A.; Isnard, O.; Pernet, M.; Wolfers, P.; Strobel, P. New model for the magnetic structure of the marokite-type oxide $CaMn_2O_4$. *J. Alloys Compd.* **2003**, *353*, 5−11.

(38) Krukau, A. V.; Vydrov, O. A.; Izmaylov, A. F.; Scuseria, G. E. Influence of the exchange screening parameter on the performance of screened hybrid functionals. *J. Chem. Phys.* **2006**, *125*, 224106.

(39) Williamson, B. A. D.; Buckeridge, J.; Chadwick, N. P.; Sathasivam, S.; Carmalt, C. J.; Parkin, I. P.; Scanlon, D. O. Dispelling the myth of passivated codoping in TiO_2. *Chem. Mater.* **2019**, *31*, 2577−2589.

(40) Williamson, B. A. D.; Limburn, G.; Watson, G. W.; Hyett, G.; Scanlon, D. Computationally driven discovery of layered quinary oxychalcogenides: Potential p-type transparent conductors. *ChemRxiv* **2019**, DOI: 10.26434/chemrxiv.7078205.v1.

(41) Einhorn, M.; Williamson, B. A. D.; Scanlon, D. Computational prediction of the thermoelectric performance of LaZnOPn (Pn = P, As). *J. Mater. Chem. A* **2020**, *8*, 7914−7924.

(42) Butler, K. T.; Hendon, C. H.; Walsh, A. Electronic chemical potentials of porous metal-organic frameworks. *J. Am. Chem. Soc.* **2014**, *136*, 2703−2706.

(43) Ganose, A. M.; Jackson, A. J.; Scanlon, D. O. Sumo: command-line tools for plotting and analysis of periodic ab-initio calculations. *J. Open Source Software* **2018**, *3*, 717.

(44) Tan, G.; Zhao, L.-D.; Kanatzidis, M. G. Rationally designing high-performance bulk thermoelectric materials. *Chem. Rev.* **2016**, *116* (19), 12123−12149.

(45) Mahan, G. D. Introduction to thermoelectrics. *Appl. Mater.* **2016**, *4*, 104806.

(46) Kim, H.-S.; Gibbs, Z. M.; Tang, Y.; Wang, H.; Snyder, G. J. Characterization of Lorenz number with Seebeck coefficient measurement. *Appl. Mater.* **2015**, *3*, 041506.

(47) Kanas, N.; Singh, S. P.; Rotan, M.; Desissa, T. D.; Grande, T.; Wiik, K.; Norby, T.; Einarsrud, M.-A. Thermoelectric properties of $Ca_3Co_{2-x}Mn_xO_6$ (x = 0.05, 0.2, 0.5, 0.75, and 1). *Materials.* **2019**, *12*, 497.

(48) Yang, J.; Youssef, M.; Yildiz, B. Predicting point defect equilibria across oxide hetero-interfaces: Model system of ZrO_2/Cr_2O_3. *Phys. Chem. Chem. Phys.* **2017**, *19*, 3869−3883.

🕮 Recommended by ACS

Oxygen Carrier and Alkali Interaction in Chemical Looping Combustion: Case Study Using a Braunite Mn Ore and Charcoal Impregnated with K_2CO_3 or Na_2CO_3

Daofeng Mei, Tobias Mattisson, *et al.*
JUNE 02, 2022
ENERGY & FUELS   READ ☑

Oxygen Nonstoichiometry and Defect Models of Brownmillerite-Structured $Ca_2MnAlO_{5+\delta}$ for Chemical Looping Air Separation

Yuan Tian, Fanxing Li, *et al.*
JULY 28, 2022
ACS SUSTAINABLE CHEMISTRY & ENGINEERING   READ ☑

Understanding the Behavior of Dicalcium Ferrite ($Ca_2Fe_2O_5$) in Chemical Looping Syngas Production from CH_4

Made Santihayu Sukma, Stuart Ashley Scott, *et al.*
AUGUST 17, 2022
ENERGY & FUELS   READ ☑

Influence of Triple Sintering Additives (BaO-CuO-B_2O_3) on the Sintering Behavior and Conductivity of the Proton-Conducting $BaZr_{0.1}Ce_{0.7}Y_{0.2}O_{3-\delta}$ Electrolyte Sintered...

Xing-Liang Lin, Cheng-Xin Li, *et al.*
APRIL 27, 2023
ACS APPLIED ENERGY MATERIALS   READ ☑

Get More Suggestions >